Finite signals in planar waveguides

Juvenal Rueda-Paz and Kurt Bernardo Wolf*

Instituto de Ciencias Físicas, Universidad Nacional Autónoma de México, Av. Universidad s/n, Cuernavaca, Morelos 62210, Mexico
**Corresponding author: bwolf@fis.unam.mx*

Received August 26, 2010; revised January 14, 2011; accepted January 25, 2011; posted February 15, 2011 (Doc. ID 134050); published March 25, 2011

We examine the evolution in phase space of an N-point signal, produced and sensed at finite arrays transverse to a planar waveguide within the framework of the finite quantization of geometric optics. We use the Kravchuk coherent states provided by the finite oscillator model to evince the nonlinear transformations that elliptic-profile waveguides produce on phase space by means of the $\mathsf{SO}(3)$ Wigner function.

OCIS codes: 070.2025, 080.2720.

1. INTRODUCTION

Consider the optical system illustrated in Fig. 1: a signal produced by a finite linear array of N phase-controlled wavefield sources that is transverse to a planar waveguide; propagating along the waveguide, the output field is sensed at a similar array of N discrete points. In geometric optics, this system produces a rotation of phase space that is not rigid beyond the paraxial regime, but involves aberrations [1]. The corresponding finite model of this system, where signals consist of N complex values assigned to equally spaced points, is obtained through the "finite quantization" process [2]. This is a unitary transformation whose "paraxial" regime is the rotation group $\mathsf{SO}(3)$, while aberrations belong to the group of $N\times N$ unitary matrices $\mathsf{U}(N)$. The purpose of this paper is to explore the correspondence between the geometric and finite waveguide models on phase space, with the aim of applying the results to compound optical setups, such as fractional Fourier transformers ([3–7], Chapter 15 in [8]), acting on pure or entangled states of light.

Finite quantization consists in "compactifying" the operators associated with the observables so that position x is assigned to a discrete spectrum. Geometric optics already has compact momentum and Hamiltonian variables, which are orthogonal projections of a vector on the Descartes circle $p^2+h^2=n^2$, where $n\equiv n(x,z)$ is the refractive index at the point $(x,z)\in\mathfrak{R}^2$; a waveguide is a medium where this index is independent of z. In Section 2, we remind the reader of the case when the waveguide profile is $n(x)^2=\nu^2-x^2$ ([8], Section 2.3), since then the three quantities x, p, and h are bound to the surface of a sphere of radius ν, and the ray trajectory is given by the rotation of the sphere around the h axis by angles proportional to z modulo 2π. If, instead, the refractive index profile has the form $n(x)^2=\nu^2-\mu^2x^2$, with $0\le\mu\le\nu$, the surface $\nu=$ constant will be an ellipsoid, and its z evolution will not be rigid.

In Section 3, we introduce the Lie algebra $\mathsf{SO}(3)$ of position, momentum, and (pseudo-)Hamiltonian operators, and their $N\times N$ matrix representations. These matrices generate the unitary transformations of our N-point signals (or act bilaterally on density matrices) and were introduced originally to build the finite oscillator model [9,10]. Its Kravchuk coherent states will serve us well here to follow the rigid rotation of the phase space sphere in the $\mu=1$ standard guide. In Section 4, we consider the generic $\mu\neq1$ case, which we place within the algebra of generators of all unitary transformations. The eigenstates of the generic elliptic-index profile waveguide satisfy a difference ("Schrödinger") equation that binds their value at every point with its second neighbors; in effect, this separates the system into two subsystems that are weakly coupled to each other, except at and near the special cases $\mu=0,1$. From the point of view of Lie theory, this is a scantly explored territory, but symbolic computation is a powerful tool to glean generic properties and solutions. In Section 5, we let a Kravchuk coherent signal travel along a (ν,μ) waveguide and examine its evolution on phase space by means of the $\mathsf{so}(3)$-covariant Wigner function [2,11,12], whose construction and main properties are succinctly described in Appendix A. We summarize some conclusions in Section 6.

2. GEOMETRIC EVOLUTION ALONG A WAVEGUIDE

In the framework of two-dimensional geometric optics referred to as Cartesian coordinates $(x,z)\in\mathfrak{R}^2$, a light ray in a generic medium of refractive index $n\equiv n(x,z)$ is a line in configuration space $\vec{r}(z)=(x(z),z)^{\mathsf{T}}$; its x coordinate measures the line chosen to be the screen, and its z coordinate is the independent parameter measuring the optical axis. The vector tangent to the ray, $\vec{p}:=\mathrm{d}\vec{r}/\mathrm{d}z=(p_x,p_z)^{\mathsf{T}}$, is constrained to a circle by the restriction $|\vec{p}\,|=n(\vec{r})$. Its x component is the optical momentum $p\equiv p_x=n\sin\theta$, where θ is the angle between the ray and the z axis, and its z component is the optical Hamiltonian function [13,14]

$$h(x,p,z)=-p_z=-n(x,z)\cos\theta=\mp\sqrt{n(x,z)^2-p^2}, \tag{1}$$

with the negative sign in the $+z$ direction. The evolution of the system is ruled by the Hamilton equations ([8], Chapters 1,2)

$$\frac{\mathrm{d}x}{\mathrm{d}z}=\frac{\partial h}{\partial p}=-\{h,x\}=\frac{p}{\sqrt{n^2-p^2}}=\tan\theta, \tag{2}$$

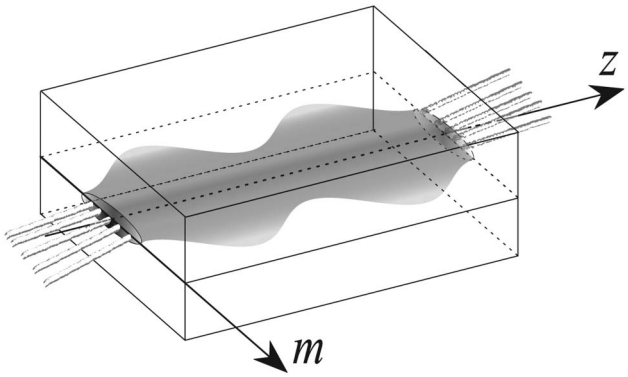

Fig. 1. Planar waveguide where a discrete signal is produced at one end by a transverse linear array of phase-controlled LEDs and read at the other end by a similar array of sensors.

$$\frac{\mathrm{d}p}{\mathrm{d}z}=-\frac{\partial h}{\partial x}=-\{h,p\}=\frac{1}{\sqrt{n^2-p^2}}\frac{\partial n^2}{\partial x}=2\frac{\partial n}{\partial x}\sec\theta, \tag{3}$$

$$\frac{\mathrm{d}h}{\mathrm{d}z}=\frac{\partial h}{\partial z}=\frac{1}{\sqrt{n^2-p^2}}\frac{\partial n^2}{\partial z}=2\frac{\partial n}{\partial z}\sec\theta, \tag{4}$$

where we recall the Poisson bracket $\{x,p\}=1$ of two functions f_1, f_2 of phase space

$$\{f_1,f_2\}(x,p):=\frac{\partial f_1}{\partial x}\frac{\partial f_2}{\partial p}-\frac{\partial f_1}{\partial p}\frac{\partial f_2}{\partial x}. \tag{5}$$

The z evolution of a ray is thus given by the solution $(x(z),p(z))$ to Eqs. (2)–(4).

In this paper, we consider only z-homogeneous waveguides where $n\equiv n(x)$, so $\partial n/\partial z=0$, and principally those whose refractive index profile is elliptic:

$$n^{\nu,\mu}(x):=+\sqrt{\nu^2-\mu^2x^2},\qquad \nu\geq 1,\mu\geq 0,\qquad |x|\leq\nu/\mu. \tag{6}$$

Since solutions exist, for mathematical ease, we have adopted the guide edges to be $x_\pm=\pm\nu/\mu$, corresponding to $n\geq 0$. (Of course, physically $n\geq 1$, implying that the actual guide edges are $\pm\sqrt{\nu^2-1}/\mu$, and with large-angle rays being lost to the surrounding medium.) Thus, at the center of the guide $n(0)=\nu$, while $1/\mu$ estimates the width of the guide. The Hamiltonian (1) in this medium has thus the form

$$h^{\nu,\mu}(x,p)=-\sqrt{\nu^2-(p^2+\mu^2x^2)}. \tag{7}$$

The z evolution of phase space in this waveguide can be then obtained, according to Eqs. (2) and (3), through the exponential of the Poisson operator $\{h^{\nu,\mu},\circ\}$, or in explicit matrix form, as

$$\begin{pmatrix}p(z)\\x(z)\end{pmatrix}=\exp(-z\{h,\circ\})\begin{pmatrix}p\\x\end{pmatrix}:=\sum_{n=0}^{\infty}\frac{(-z)^n}{n!}\{h,\circ\}^n\begin{pmatrix}p\\x\end{pmatrix}, \tag{8}$$

$$=\begin{pmatrix}\cos(\mu z/h(x,p)) & -\mu\sin(\mu z/h(x,p))\\ \sin(\mu z/h(x,p))/\mu & \cos(\mu z/h(x,p))\end{pmatrix}\begin{pmatrix}p\\x\end{pmatrix}, \tag{9}$$

where $\{h,\circ\}^n:=\{h,\{h,\circ\}^{n-1}\}$, $\{h,\circ\}^1:=\{h,\circ\}$, $\{h,\circ\}^0:=1$, and $h\equiv h^{\nu,\mu}$. The evolution of phase space will be that of an incompressible fluid flowing along the ellipses $p^2+\mu^2x^2=$ constant, with minor half-axis 1 along p, and major half-axis $1/\mu$ along x (see Fig. 2). The center $p=0=x$ corresponds to the standard ray along the waveguide axis, while the boundary contains the extreme rays that touch tangentially the $|x|=\nu/\mu$ edge.

Rays near to the standard ray, $p^2+\mu^2x^2\ll\nu^2$, allow the paraxial approximation to Eqs. (8) and (9):

$$\exp\left(\frac{-z}{2\nu}\{p^2+\mu^2x^2,\circ\}\right)\begin{pmatrix}p\\x\end{pmatrix}=\begin{pmatrix}\cos(\mu z/\nu) & -\mu\sin(\mu z/\nu)\\ \sin(\mu z/\nu)/\mu & \cos(\mu z/\nu)\end{pmatrix}\begin{pmatrix}p\\x\end{pmatrix}. \tag{10}$$

This is equivalent to the time–z evolution of a particle of mass ν in the harmonic oscillator potential $\frac{1}{2}\mu^2x^2/\nu$. Finally, in the special case $\mu\to 0$ when the waveguide becomes a homogeneous medium, its evolution (9) is free flight:

$$\begin{pmatrix}p(z)\\x(z)\end{pmatrix}=\begin{pmatrix}1 & 0\\ z/\sqrt{\nu^2-p^2} & 1\end{pmatrix}\begin{pmatrix}p\\x\end{pmatrix}=\begin{pmatrix}p\\ x+zp/\sqrt{\nu^2-p^2}\end{pmatrix}. \tag{11}$$

In this case, forward rays ($|\theta|<\frac{1}{2}\pi$) have energies in the range $-\nu<h^{\nu,0}<0$ and backward rays in the range $0<h^{\nu,0}<\nu$.

3. FINITE QUANTIZATION AND KRAVCHUK COHERENT STATES

The finite quantization of a classical system to a wave system whose position spectrum is discrete and finite is based on the Lie algebra $\mathsf{so}(3)$ and leads to the finite model of the harmonic oscillator [10]. Both the classical and the finite models satisfy the Hamilton equations of the harmonic oscillator. For the classical model, they involve the Poisson brackets between

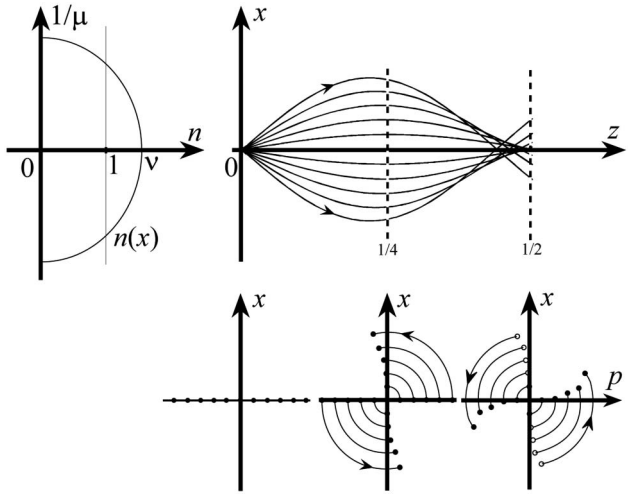

Fig. 2. Top left, refractive index $n^{\nu,\mu}(x)$ of an elliptic-index profile waveguide [Eq. (6)]; the mathematical boundary is $n^{\nu,\mu}=0$, while the physical one is $n=1$. Top right, rays starting from the center of the guide at various angles $p=\nu\sin\theta<\nu$; these trajectories do not reconvene at a single point, so this guide is dispersive. Bottom, evolution of the phase space points $(p(z),x(z))$ for $\frac{1}{4}$ and $\frac{1}{2}$ cycle of the paraxial period [Eq. (10)], $z=\nu/2\pi\mu$.

position x, momentum p, and the classical oscillator Hamiltonian $k:=\frac{1}{2}(p^2+x^2)$:

$$\{k,x\}=-p, \qquad \{k,p\}=x. \tag{12}$$

On the other hand, for the finitely quantized model [10,15], the Lie bracket is the commutator between operators of position $\mathcal{X}$, momentum $\mathcal{P}$, and a pseudo-Hamiltonian $\mathcal{K}$, for which we assume no specific form. Corresponding to Eq. (12), the two Hamilton equations are

$$[\mathcal{K},\mathcal{X}]=-i\mathcal{P}, \qquad [\mathcal{K},\mathcal{P}]=i\mathcal{X}. \tag{13}$$

These operators are required to be self-adjoint in an appropriate complex Hilbert space (below) such that the spectrum of observable positions are a finite set of equally spaced values. This requirement is met through deformation of the basic Poisson bracket $\{x,p\}=1$ of the classical model into

$$[\mathcal{X},\mathcal{P}]=-i\mathcal{K}. \tag{14}$$

With this postulate, the three operators $\mathcal{X}$, $\mathcal{P}$, and $\mathcal{K}$ become the generators of the Lie algebra $\mathsf{so}(3)$, best known for its use in quantum angular momentum theory.

The representations of the algebra $\mathsf{so}(3)$ by self-adjoint operators can be completely reduced and characterized as eigenspaces of the Casimir operator [16,17]:

$$\mathcal{C}:=\mathcal{X}^2+\mathcal{P}^2+\mathcal{K}^2=j(j+1)1, \tag{15}$$

whose eigenvalues (numbered by $j\geq 0$) are integers and determine the vector space to be of dimension $N=2j+1$. In this way, the eigenvalues of all three operators, $\mathcal{X}$, $\mathcal{P}$, and $\mathcal{K}$, which we shall indicate by $x_m\equiv m$, ϖ and κ, respectively, will range over the integers between $-j$ and j. (For half-integer js, one has the homomorphic algebra $\mathsf{su}(2)$, but, because for N even there will be no sensor at the center of the array $x_0=0$ nor a standard ray $\varpi=0$, we shall consider odd Ns only.)

The position, momentum, and pseudo-Hamiltonian in the finite oscillator model are thus represented by $N\times N$ matrices $(N=2j+1)$ that belong to the representation j of $\mathsf{so}(3)$: $x\sim\mathbf{X}=\|X_{m,m'}\|$, $p\sim\mathbf{P}=\|P_{m,m'}\|$, and $h\sim\mathbf{K}=\|K_{m,m'}\|$. Their elements are obtained [17] from the commutation relations (13) and (14):

$$X_{m,m'}=m\delta_{m,m'}, \qquad m,m'\in\{-j,-j+1,\ldots,j\}, \tag{16}$$

$$\begin{aligned}P_{m,m'}=&-i\frac{1}{2}\sqrt{(j-m)(j+m+1)}\,\delta_{m+1,m'}\\&+i\frac{1}{2}\sqrt{(j+m)(j-m+1)}\,\delta_{m-1,m'},\end{aligned} \tag{17}$$

$$\begin{aligned}K_{m,m'}=&\frac{1}{2}\sqrt{(j-m)(j+m+1)}\,\delta_{m+1,m'}\\&+\frac{1}{2}\sqrt{(j+m)(j-m+1)}\,\delta_{m-1,m'},\end{aligned} \tag{18}$$

and are well known as the $\mathsf{so}(3)$ irreducible representation matrices. They are Hermitian and traceless, and their sum of squares [Eq. (15)] is a multiple of the unit matrix

$$\mathbf{C}:=\mathbf{X}^2+\mathbf{P}^2+\mathbf{K}^2=j(j+1)\mathbf{1}. \tag{19}$$

The proper Hilbert space for finite models is thus C^N, consisting of N-component column vectors $\mathbf{f}=\{f_m\}_{m=-j}^{j}$ whose elements are the complex values of the N-point signals, endowed with the usual sesquilinear inner product and norm:

$$(\mathbf{f},\mathbf{g})\equiv\mathbf{f}^\dagger\mathbf{g}=\sum_{m=-j}^{j}f_m^*g_m=(\mathbf{g},\mathbf{f})^*, \qquad |\mathbf{f}|=\sqrt{(\mathbf{f},\mathbf{f})}. \tag{20}$$

Position is represented by a diagonal matrix $\mathbf{X}$ in Eq. (16); momentum $\mathbf{P}$ in Eq. (17) is $-i$ times a weighted central difference, and the pseudo-Hamiltonian matrix $\mathbf{K}$ in Eq. (18) is real and symmetric. They all have orthogonal eigenbases, two of which are of immediate interest: the position (Kronecker) basis $\{\mathbf{x}_m\}_{m=-j}^{j}$ and the (pseudo-)energy basis $\{\mathbf{k}_\kappa\}_{\kappa=-j}^{j}$, which satisfy

$$\mathbf{X}\mathbf{x}_m=x_m\mathbf{x}_m, \qquad \mathbf{K}\mathbf{k}_\kappa=\kappa\mathbf{k}_\kappa. \tag{21}$$

Their overlaps are the finite oscillator wave functions [9,18]

$$\Phi_n^j(x_m):=(\mathbf{x}_m,\mathbf{k}_{n-j})=d^j_{n-j,m}\left(\frac{1}{2}\pi\right), \tag{22}$$

$$(\mathbf{x}_m,\mathbf{K}\Phi_n^j)=\kappa\Phi_n^j(x_m), \tag{23}$$

where $n:=\kappa+j$, $n|_0^{2j}$, and $m|_{-j}^{j}$, and $d^j_{\kappa,m}(\theta)$ is the well-known Wigner little-d function ([18], Section 3.6) of angle $\frac{1}{2}\pi$ on the Casimir sphere (15) between $\mathcal{X}$ and $\mathcal{K}$, and $\kappa=n-j$. The explicit expression of $\Phi_n^j(m)$ is the square root of a binomial distribution times a Kravchuk polynomial of degree $n=\kappa+j$ in m [19–21]. We called them the Kravchuk oscillator functions [9]:

$$\begin{aligned}\Phi_n^j(x_m)&=\frac{(-1)^n}{2^j}\sqrt{\binom{2j}{n}\binom{2j}{j+m}}K_n\left(j+m;\frac{1}{2},2j+1\right)\\&=\Phi_m^j(x_n).\end{aligned} \tag{24}$$

Please note that these functions are eigenfunctions of $\mathbf{K}$ and not of $\frac{1}{2}(\mathbf{P}^2+\mathbf{X}^2)$; yet, for $j\to\infty$, they limit to the standard Hermite–Gauss functions [22].

The one-parameter Lie group generated by $\mathbf{K}$ rotates the real three-dimensional space $(u,v,w)\in\mathfrak{R}^3$ of coefficients of the generic Lie algebra element $u\mathbf{X}+v\mathbf{P}+w\mathbf{K}$ around the w axis; it is the group $\mathsf{SO}^{\mathrm{K}}(2)\subset\mathsf{SO}(3)$. In the Hilbert space C^N, this group is represented by $N\times N$ unitary matrices known from standard results of angular momentum theory [17,23]:

$$\mathbf{U}^{\mathrm{K}}(z):=\exp(iz\mathbf{K})\in\mathsf{U}(\mathsf{N}), \tag{25}$$

$$U^{\mathrm{K}}_{m,m'}(z)=i^{m-m'}d^j_{m,m'}(z)=e^{-ijz}\sum_{n=0}^{2j}\Phi_n^j(x_m)e^{inz}\Phi_n^j(x_{m'}) \tag{26}$$

with z modulo 2π and $n=\kappa+j$ as before. In fact, Eq. (26) are the matrix elements of the Fourier–Kravchuk transform

kernel introduced in [9] and further analyzed and compared with other discrete fractional Fourier transforms in [23]. The z evolution of the Kravchuk functions $\Phi_n^j(x_m)$ in Eq. (22) multiplies them by the phase e^{inz}.

In particular, the $n=0$ Kravchuk ground and $n=2j$ top states of Eq. (22) are

$$\Phi_0^j(x_m)=\frac{1}{2^j}\sqrt{\binom{2j}{j+m}}=(-1)^m\Phi_{2j}^j(x_m)>0. \tag{27}$$

The set of C^N vectors that exhibit the classical oscillator motion under Eq. (25) are the Kravchuk coherent states, defined in [10] as the ground state Φ_0^j in Eq. (27), rotated over the sphere $x^2+p^2+\kappa^2=r^2$. A selection of these states is shown in Fig. 3. Rotations around the p axis will raise the "bottom pole" $\kappa=-r$ up along the meridian in the x–κ plane by angles $\theta|_0^\pi$; this yields the family of coherent states

$$\Upsilon_\theta^j(x_m)\coloneqq\sum_{m'=-j}^{j}(\exp(i\theta\mathbf{P}))_{m,m'}\Phi_0^j(x_{m'})=d^j_{-j,m}\left(\frac{1}{2}\pi+\theta\right), \tag{28}$$

with $\Upsilon_0^j(x_m)=\Phi_0^j(x_m)$. Under the $\mathsf{SO}^{\mathrm{K}}(2)$ rotations generated by $\mathbf{K}$, the sphere will rotate by angles $\phi=z$ modulo 2π, carrying around the coherent state, and thus associating one Kravchuk coherent state $\Upsilon^j_{(\theta,\phi)}(x_m)$ to every point (θ,ϕ) of the sphere in Fig. 3.

The purpose of this section is to present the finite harmonic oscillator model [10] in the robes of the Kravchuk guide, using the fact that, from Eq. (19), we can write the matrix $\mathbf{K}$ in the form

$$\mathbf{K}=\pm\sqrt{j(j+1)\mathbf{1}-(\mathbf{P}^2+\mathbf{X}^2)}. \tag{29}$$

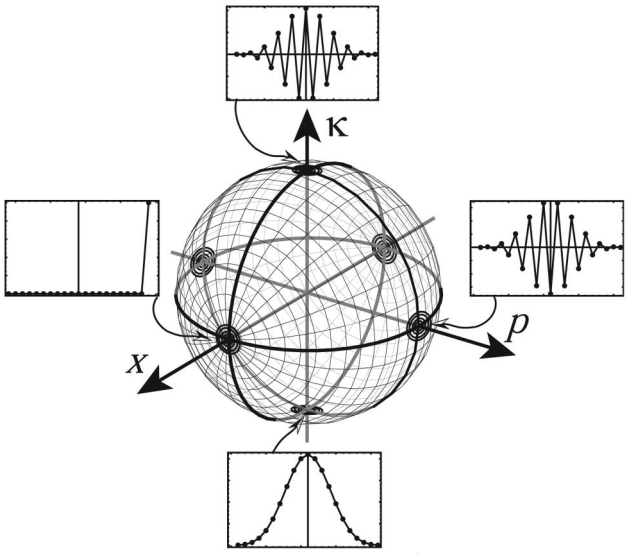

Fig. 3. Sphere of Kravchuk coherent states $\Upsilon^j_{(\theta,\phi)}(x_m)$ in Eq. (28). This is also the phase-space representation of the finite system, with the axes of position x, momentum p, and pseudoenergy κ (see Appendix A). At the bottom pole, $\kappa=-r$ is the ground state $\Upsilon^j_0(x_m)=\Phi^j_0(x_m)$, and, at the top pole, $\kappa=r$ is the top state $\Upsilon^j_\pi(x_m)=\Phi^j_{2j}(x_m)$. At the $+x$ pole, the state $\Upsilon^j_{\pi/2}(x_m)$ is the Kronecker state $(0,\ldots,0,1)$; at the $+p$ pole, it is the z evolution of the latter after a $\frac{1}{4}$ cycle, $z=\frac{1}{2}\pi$.

Comparing with Eq. (7), we see that this Kravchuk guide corresponds to a classical guide where $\nu=1=\mu$. This will be our reference guide for all other elliptic-profile $n^{\nu,\mu}(x)$ guides [Eq. (6)]; it will serve also for generic $n(x)$ profile waveguides (1) to be investigated later. Still, only the Kravchuk coherent states in their guide [Eq. (29)] will recover their exact initial form under $\mathbf{U}^{\mathrm{K}}(2\pi)=\mathbf{1}$. Note carefully that this harmonic motion is the result of the rotation of the sphere, rather than of the dynamics of a mechanical oscillator. In Fig. 4, we show the $\mathsf{SO}^{\mathrm{K}}(2)$ evolution of a $\theta=1$ radian Kravchuk coherent state over one cycle $z|_0^{2\pi}$. The transformation of this signal is displayed most visibly by its $\mathsf{SO}(3)$–Wigner function on the phase space of the finite system, whose definition and properties are condensed in Appendix A.

4. FINITE WAVEGUIDE MODELS

The correspondence between classical systems and their finite-quantized counterparts is postulated to result from the association between functions $F(x,p)$ in the former, with Weyl-ordered [2] matrices $\mathbf{F}=F(\mathbf{X},\mathbf{P})_{\mathrm{Weyl}}$ in the latter. The elliptic-profile waveguide Hamiltonian $h^{\nu,\mu}(x,p)$ in Eq. (7) will be thus finitely quantized to an $N\times N$ Hermitian matrix of the form (29)

$$\mathbf{H}^{\nu,\mu}\coloneqq\sqrt{\nu^2\mathbf{C}-(\mathbf{P}^2+\mu^2\mathbf{X}^2)}=-\sqrt{[(\nu^2-1)\mathbf{C}-(\mu^2-1)\mathbf{X}^2]+\mathbf{K}^2}, \tag{30}$$

where we note that between brackets in Eq. (30) is a diagonal matrix, and that the Weyl ordering is not really needed here—provided that a cogent square-root operation for the radicand is used, since, at least for the Kravchuk case, the resulting $\mathbf{K}=\sqrt{\mathbf{K}^2}$ has both positive and negative eigenvalues.

To make proper sense of the square root in Eq. (30) [24], we should first examine the square Hamiltonian $\mathbf{H}^2\equiv(\mathbf{H}^{\nu,\mu})^2$. We indicate is normalized eigenfunctions and eigenvalues by

$$\mathbf{H}^2\Psi_n=(\eta_n)^2\Psi_n,\qquad \Psi_n(x_m)=(\mathbf{x}_m,\Psi_n), \tag{31}$$

with $n|_0^{2j}$, $m|_{-j}^{j}$ as before, and (ν,μ) implied. We clarify first the matter of scales in position and energy. Because the eigenvalues of $\mathbf{X}$ range in $x_m\equiv m|_{-j}^{j}$, while the classical coordinate x ranges in $|x|\le\nu/\mu$, if we set $x\leftrightarrow x_m/j\equiv m/j$, the points of the sensor array will be measured by $x\in[-1,1]$. When $\mu<\nu$, the array fits inside the ellipse of the refractive index in Fig. 2; when $\mu=\nu$, it spans the full mathematically allowed range, and, finally, if $\mu>\nu$, the array would stick into imaginary $n(x)$ regions and this model would be unphysical. We should thus restrict the waveguide parameters to $0\le\mu\le\nu\ge1$.

Concerning energy h in Eq. (7), we saw that its classical range is $h|_{-\nu}^{0}$ for forward rays $-\frac{1}{2}\pi<\theta<\frac{1}{2}\pi$ (and $h|_0^\nu$ for backward rays $\frac{1}{2}\pi>\theta>\frac{3}{2}\pi$). The lowest value $h=-\nu$ characterizes the standard ray $\theta=0$ along the center of the guide, and $h=0$ corresponds to the extreme rays that are tangent to the guide boundary $|x|=\nu/\mu$. In the Kravchuk guide [Eq. (29)], where $\mu=1=\nu$, the ground and top states [Eq. (27)] are degenerate under $\mathbf{K}^2$ with eigenvalue $(\mp j)^2$. (We can easily generalize to $\nu\ge1$ because only a constant is added.) In the special case $\mu=1$, the ground and top states of $(\mathbf{H}^{\nu,1})^2$ in Eq. (31) have eigenvalues $(\eta_0)^2=(\eta_{2j})^2\approx(\nu j)^2$ for large j, so the scale in Eq. (30) is consistent. However,

we must be careful to assign the negative sign to the ground state, so $\eta_0 \approx -\nu j$, and the positive one for the top $\eta_{2j} \approx \nu j$. The other special case is $\mu = 0$, where the nondiagonal part of the radicand, $\mathbf{K}^2$ in Eq. (30), is now $-\mathbf{P}^2$; the ground state then corresponds to the zero-momentum state $\varpi = 0$ whose energy, $h = -\nu$, identifies the only nondegenerate state.

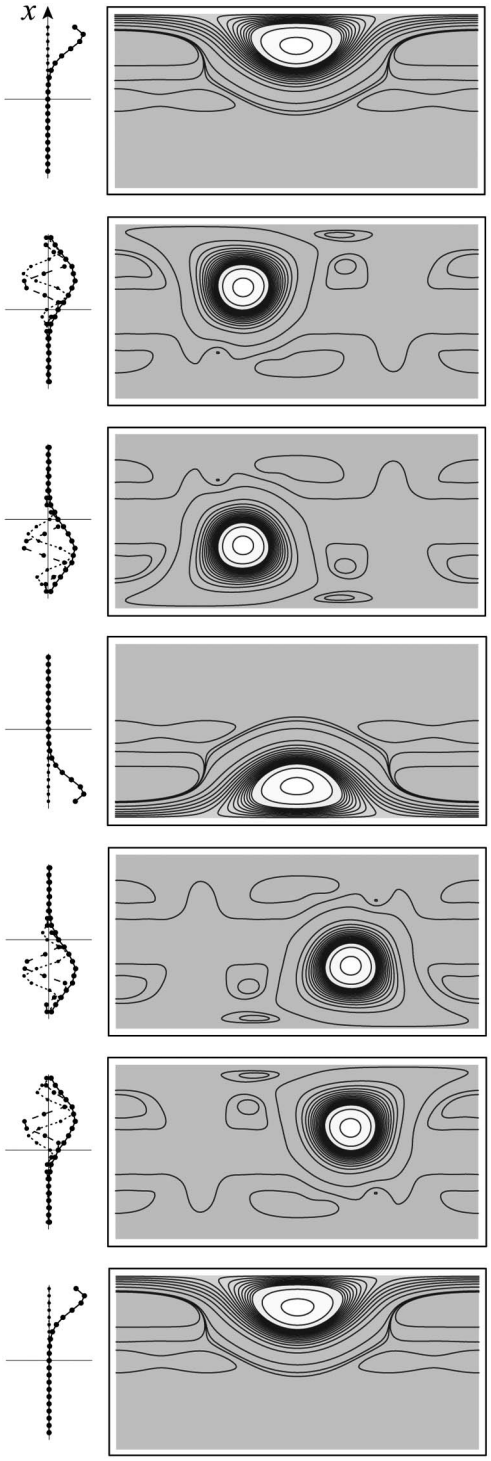

Fig. 4. Evolution under $\mathbf{U}^{\mathrm{K}}(z)$ of the coherent state $\Upsilon^j_\theta(m)$ for $j = 10$ and $\theta = 1$ radian. Top to bottom, $z = \frac{1}{3}\pi n$, $n = 0, 1, \ldots, 6$. Left, each signal on a vertical x_m axis; right, the corresponding $\mathsf{SO}(3)$–Wigner function (see Appendix A). For visibility, the real, imaginary, and absolute values of the discrete signal points are joined by dashed, dotted, and continuous curves, respectively.

The matrices $\{\mathbf{X}, \mathbf{P}, \mathbf{K}\}$, in addition to hermiticity across the main diagonal, also exhibit symmetry $\{-, +, +\}$ under reflection across their antidiagonals, and hence so do their squares. Thus, $\mathbf{H}^2 - \nu^2\mathbf{C}$ is symmetric across both diagonals, with j pairwise degenerate eigenvalues. Moreover, since $\mathbf{K}$ and $\mathbf{P}$ are bidiagonal (having nonzero matrix elements at $m = m' \pm 1$), it follows that $\mathbf{H}^2$ will be tridiagonal (nonzero at $m = m'$ and $m = m' \pm 2$), its off-diagonal elements being independent of ν, μ, with a checkerboard of zeros for all odd $m - m'$. Lie theory is well acquainted with recursion relations, such as implied by Eq. (23), which become the difference equation satisfied by the Kravchuk functions $\Phi^j_n(x_m)$ in Eq. (22), that bind the values of the eigenfunctions at three neighboring points x_m and $x_{m\pm1}$ [with $\Phi^j_n(x_{\pm(j+1)}) \equiv 0$]. Thus, $\mathbf{H}^2$ in Eq. (31) yields a step-two difference equation:

$$\begin{aligned}&\frac{1}{4}\sqrt{(j-m-1)(j-m)(j+m+1)(j+m+2)}\,\Psi_\eta(m+2)\\&\quad+\left[j(j+1)\left(\nu^2-\frac{1}{2}\right)-m^2\left(\mu^2-\frac{1}{2}\right)-\eta^2\right]\Psi_\eta(m)\\&\quad+\frac{1}{4}\sqrt{(j+m-1)(j+m)(j-m+1)(j-m+2)}\,\Psi_\eta(m-2)\\&\quad=0.\end{aligned} \tag{32}$$

This is, in effect, a pair of difference equations: one for the points x_m with even ms and one for odd ms. Since both are invariant under $m \leftrightarrow -m$, their solutions for $\pm\eta$ can be chosen to have definite parities.

We recall that, in the Kravchuk guide $\mu = 1 = \nu$, the $2j + 1$ eigenvalues $\{\kappa^2\}$ of $\mathbf{K}^2$ contain one nondegenerate midstate $\kappa = 0$ and j degenerate pairs, each with the positive eigenvalue $(\pm\kappa)^2$. Their square roots, being the eigenvalues of $\mathbf{K}$, will disentangle the pairs by a sign: negative for the lower states, and positive for the higher ones. In Fig. 5, we show the computed eigenvalues $\{(\eta^{\nu,\mu})^2\}$ of $(\mathbf{H}^{\nu,\mu})^2$, $0 \le \mu \le \nu$, for the Kravchuk case $\nu = 1$ and for $\nu = \sqrt{2}$, the latter being a representative of the generic case. The spectra of the square operators show j degenerate pairs at $\mu = 0$ and $\mu = 1$; in between, the partners are exchanged. We observe that the largest square eigenvalue, $\max_{0\le n\le 2j}\eta_n^2$, corresponds to the ground state η_0 with a negative sign, the second-highest square eigenvalue corresponds to the top state η_{2j} with a positive sign, the third-highest square eigenvalue gives η_1 again with a negative sign, the fourth-highest is η_{2j-1}, etc., alternating signs thereafter down to the midstate η_j. In Fig. 5, we show the spectra of $\mathbf{H}^{\nu,\mu}$ constructed with the square roots of the former and the same alternating-sign scheme. The fact that the eigenvalue lines do not cross gives credence to the consistency of this scheme.

Let us now turn to the eigenvectors, with the caveat that several conclusions are based on numerical computation rather than analytic proof. The real orthogonal matrix of eigenvectors of $(\mathbf{H}^{\nu,\mu})^2$, $\Psi := \{\Psi_n(x_m)\}$ satisfying Eq. (32) shows a quick but continuous transition from the matrix of Kravchuk functions $\Phi := \{\Phi_n(x_m)\}$ for $\mu = 1$, developing a checkerboard of very small elements. Indeed, for $j = 10$, $\nu = \sqrt{2}$ when $|\mu - 1| > 0.1$ and also when $\mu > 0.4$; all of these elements have magnitude $< 1.5 \times 10^{-4}$, so the matrix of eigenvectors has practically a checkerboard of zeros. However, this means, in turn, that plots of these finite waveguide modes will have a

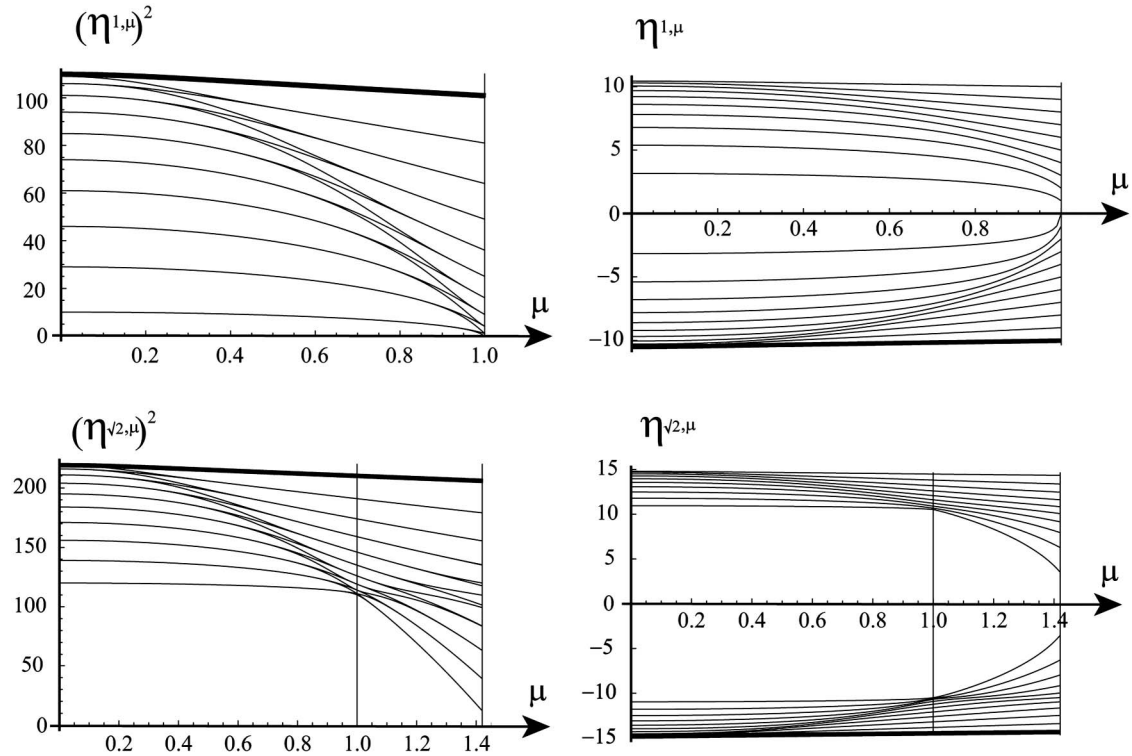

Fig. 5. Eigenvalues of the Hamiltonian matrices and their squares for $0 \le \mu \le \nu$. Top row, $\nu = 1$ (the Kravchuk guide); bottom row, $\nu = \sqrt{2}$ for $j = 10$ ($N = 21$ points). Left column, squared eigenvalues $\{(\eta^{\nu,\mu})^2\}$ of the squared matrices $(\mathbf{H}^{\nu,\mu})^2$. Right column, eigenvalues $\{\eta^{\nu,\mu}\}$ of the matrices $\mathbf{H}^{\nu,\mu}$ with the sign assignment scheme given in the text. The ground state eigenvalues $(\eta_0^{\nu,\mu})^2$ and $\eta_0^{\nu,\mu}$ are marked with a heavy curve. Note that, once separated by the sign, the $\eta_n^{\nu,\mu}$ curves do not cross. Only the Kravchuk case $\nu = 1 = \mu$ has equally spaced eigenvalues.

"porcupine" appearance, being very close to zero at every even or every odd point. In particular, corresponding to the two highest η_n^2 values (the ground and top states), the two eigenvectors $\Psi_{j\mp j}(x_m)$ have the characteristic bell-shaped envelope of the ground state $\Phi_0(x_m)$, one near zero at odd ms and the other at the even ms. Yet, as we show in Fig. 6, their sum and difference,

$$\tilde{\Psi}_0(x_m) := \Psi_0(x_m) + \Psi_{2j}(x_m), \tag{33}$$

$$\tilde{\Psi}_{2j}(x_m) := \Psi_0(x_m) - \Psi_{2j}(x_m), \tag{34}$$

resemble most closely the Kravchuk ground and top states. We may call them pseudo-ground and pseudo-top states. Thus, we have the remarkable situation that, in the generic finite waveguide, the ground and top states are actually superpositions of two eigenfunctions with slightly different eigenvalues of square energy.

To finish our quest for the Hamiltonian matrix $\mathbf{H}^{\nu,\mu}$ in Eq. (30), we use the matrix of eigenvectors $\Psi = \{\Psi_n(x_m)\}$ to diagonalize $\mathbf{H}^2$ to $\mathbf{D}^2$, take the square root of the latter's elements (with the proper sign according to the previous scheme) to build $\mathbf{D}$, and, finally, use the inverse of the same eigenvector matrices on this $\mathbf{D}$ to restore the matrix to $\mathbf{H}$ in the position basis $(x_m, x_{m'})$. Thus,

$$\Psi^\dagger \mathbf{H}^2 \Psi = \mathbf{D}^2, \qquad \mathbf{H}^{\nu,\mu} := \Psi \mathbf{D} \Psi^\dagger, \qquad \mathbf{H}^{\nu,\mu} \Psi_n = \eta_n \Psi_n. \tag{35}$$

It is straightforward to compute these matrices numerically, and again we note that they contain a checkerboard of near-zero elements in the ranges detailed above, which effectively

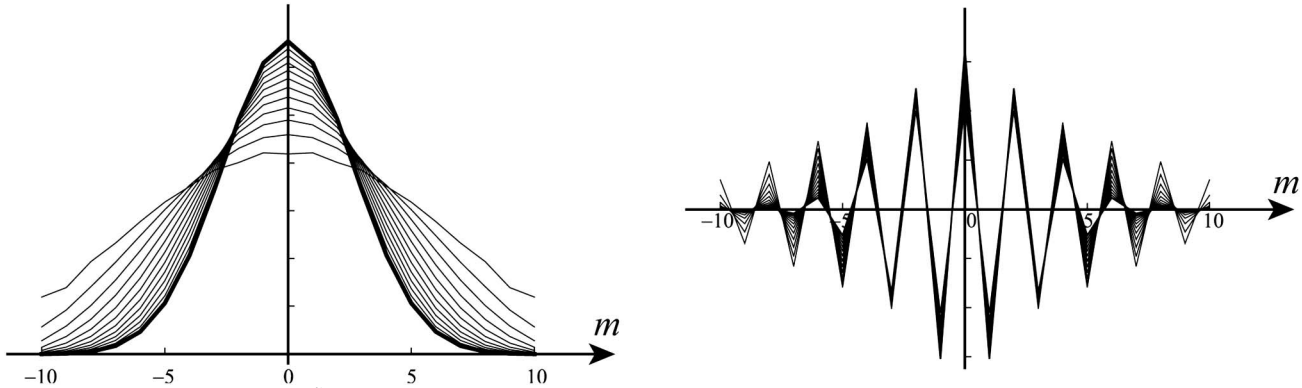

Fig. 6. Left, pseudoground states $\tilde{\Psi}_0(x_m)$ in Eq. (33) for $j = 10$, $\nu = \sqrt{2}$ (for visibility, point values are joined by straight lines), and values of $\mu = 0.4, 0.5, \ldots, 1.3$, and $\mu = \sqrt{2}$ marked with a heavy line. Right, pseudotop states $\tilde{\Psi}_{2j}(x_m)$ in Eq. (34) for the same values of the parameters. Kravchuk ground and top states lie at $\mu = 1$. Note that widths grow as the waveguide becomes wider (μ decreases).

separate the matrix elements of the finite $(2j+1)$-dimensional waveguide system into two independent subsystems, of dimensions $j+1$ for the odd m points $\{x_m\}$ and j for the even m ones. Whether this feature can be dynamically justified or is an artifact of the square-root operation is among the questions we defer to future work. In Section 5, we use the matrix $\mathbf{H}^{\nu,\mu}$ found in Eq. (35) to generate the evolution of signals provided by the finite waveguide model.

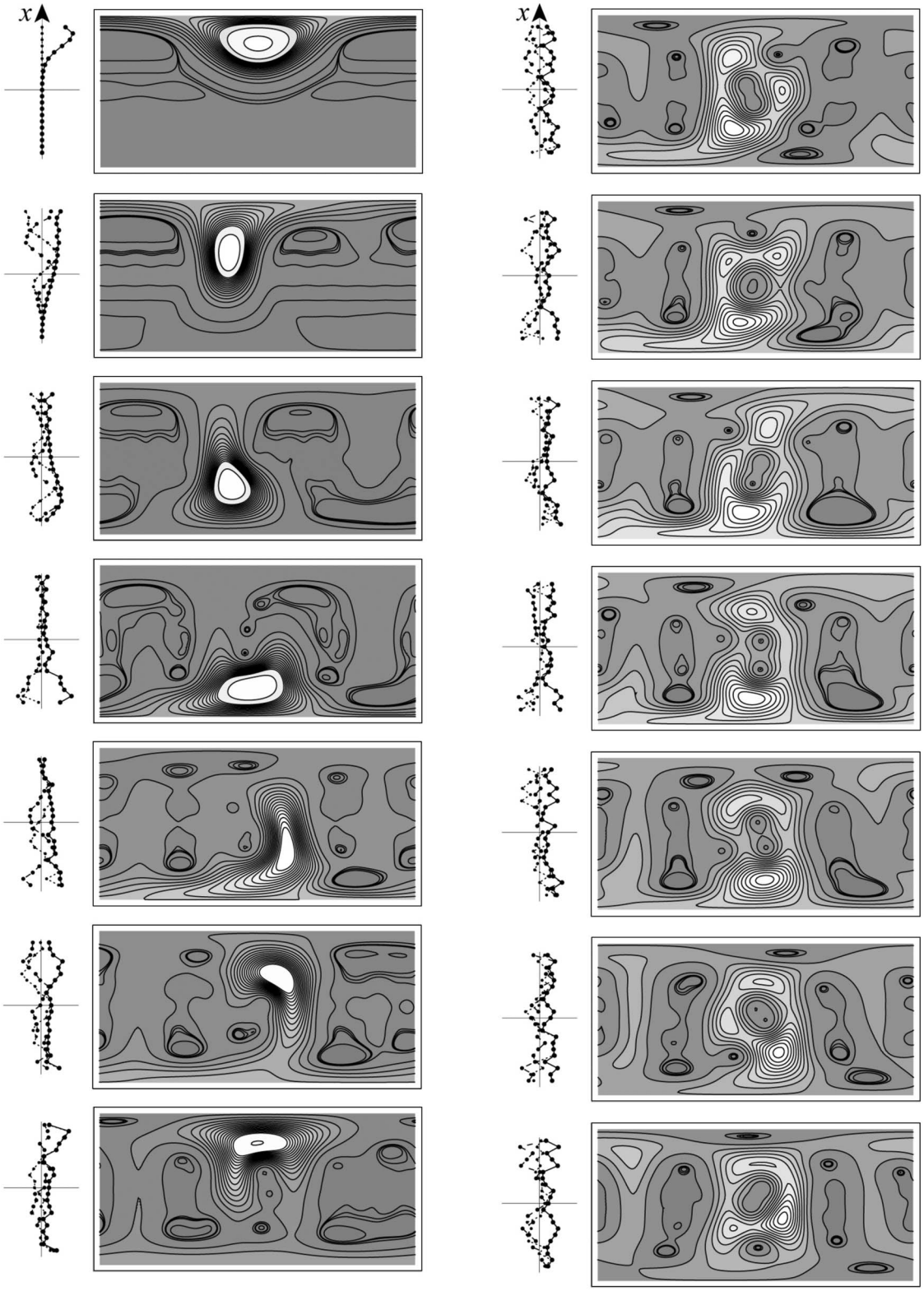

Fig. 7. Evolution of the Kravchuk coherent state $\Upsilon^j_\theta(m)$ for $\theta = 1$ radian and $j = 10$ under the waveguide Hamiltonian $\mathbf{H}^{\nu,\mu}$ in Eq. (30) for $\nu = \sqrt{2}$ and $\mu = \frac{1}{2}\sqrt{2}$. Markings for the signals and its Wigner functions are the same as in Fig. 4. In the left column, we show one approximate cycle for $z = \frac{1}{3}\pi c n$, $n = 0, 1, \ldots, 6$, with the scale factor $c = 2.8284$. After several oscillations, in the right column, we show a sequence of two- and three-component catlike states for $z = \frac{1}{16}315\pi + \frac{3}{16}\pi n$.

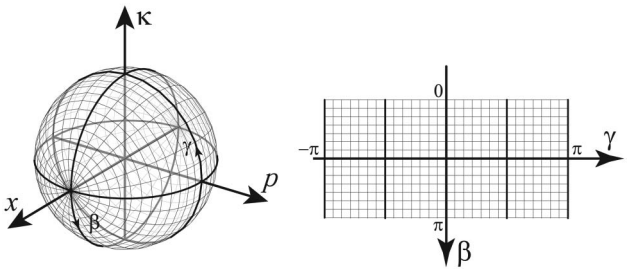

Fig. 8. Left, polar coordinates (β,γ) of the sphere refer to the x axis of positions. Right, projection of the coordinates (β,γ) of the sphere onto the rectangle $(0\le\beta\le\pi,-\pi<\gamma\le\pi)$. In this projection, the bottom pole $(\frac{1}{2}\pi,0)$ is at the center of the rectangle, the x axis of positions is vertical; the boundary $(0,\gamma)$ represents the single point x_j and (π,γ) represents x_{-j}. The p axis of momenta is horizontal, with its left and right boundaries identified, so the top pole corresponds to $(\frac{1}{2}\pi,\pi)\equiv(\frac{1}{2}\pi,-\pi)$. The heavy lines divide phase space into octants.

5. EVOLUTION ALONG DISCRETE GUIDES

The evolution of an N-point signal in the model that we have pursued in this paper is given by the one-parameter group of $N\times N$ unitary matrices

$$\mathbf{U}^{\nu,\mu}(z):=\exp(iz\mathbf{H}^{\nu,\mu})\in\mathsf{U}(N), \tag{36}$$

generated by $\mathbf{H}^{\nu,\mu}$ in Eq. (35) with ν,μ in the appropriate ranges. Within the N^2-dimensional real manifold of $\mathsf{U}(N)$, this is a line parametrized by $z\in\mathfrak{R}$. Since the eigenvalues of $\mathbf{H}^{\nu,\mu}$ are generally incommensurable for $0<\mu<\nu$, the subgroup line is a Lissajous figure in that manifold, and no proper period can be defined; only for the Kravchuk guide does this line close into a circle.

Note that, when we act with Eq. (36) on the matrices of the $\mathsf{so}(3)$ algebra as $\mathbf{U}^{\nu,\mu}(z)\mathbf{X}\mathbf{U}^{\nu,\mu}(-z)$, etc., we produce Hermitian matrices that are not linear combinations of those $\mathsf{so}(3)$ generators. Indeed, the transformation Eq. (36) represents a nonlinear map of the algebra $\mathsf{so}(3)$ that spills over into the algebra $\mathsf{u}(N)$ of all Hermitian $N\times N$ matrices. On the N-point signal vectors, this represents aberrations. For finite systems, there are only N^2-4 aberrations, which have been classified in [2], but await application. Figure 4 depicts the evolution of a Kravchuk coherent states under the Kravchuk guide, which was a purely group-theoretical construction. This can be now compared with the evolution of the same Kravchuk coherent state under the elliptic-profile waveguide [Eq. (36)] in Fig. 7, shown with its Wigner function. We notice the same general circular movement, but soon enough the peak smears until it reaches its tail and starts interfering with itself to produce Schrödinger catlike states. These are most readily resolved with the $\mathsf{SO}(3)$ Wigner function on phase space, but would be difficult to identify by looking only at the signal.

6. CONCLUSIONS AND EXTENSIONS

The square-root form of the waveguide Hamiltonian (30) indicates that the analysis of the finite system under consideration differs in crucial aspects from the previously studied systems: the finite oscillator on $\mathsf{so}(3)$ [9,10], the discrete-free particle [15,25] on $\mathsf{iso}(3)$, and the discrete repulsive oscillator on $\mathsf{so}(2,1)$ [15,26], whose Hamiltonians are elements of their algebras. A consequence of the square-root operation is the need to assign signs to the eigenvalues. Had we not done so in Eq. (35), the eigenvectors would have their signs reversed at odd m sensor points, and the unitary evolution matrix (36) would suffer complex conjugation at those points. Although in a very different context, the Dirac equation resolves the square root of an operator through unfolding the Hilbert space of wave functions into four copies of itself. An important conclusion of our work is that the classical property of canonicity in Eq. (8) became that of unitarity of Eq. (36) on the space C^N of N-point complex signals.

We would like to put our endeavours in the context of optical systems used to transform finite N-point signals and detect or correct aberrations. The elliptic refractive index profile $\nu^2-\mu^2x_m^2$ in Eq. (1) was chosen in this paper for its parametric proximity to the $\mathsf{so}(3)$ Kravchuk guide, but $n(x)$ can be given any shape when represented by a diagonal matrix of elements $n(x_m)$ for $m|_{-j}^{j}$, including discrete rectangular or two-channel profiles. Further, two waveguides with different profiles placed end to end with a flat interface will perform as the product of their evolution matrices, ordered from left to right. Free flights in a finite system are $\mu=0$ guides, and should not be too long if they are to mimick the Fresnel transform [27]. To incorporate other elements, such as lenses, thin or with geometric aberrations, a parallel strategy can be followed [2], replacing the ordered product of exponentiated Poisson operators that characterize such elements ([8], Chapter 14) by their $\mathsf{so}(3)$ Weyl-ordered counterparts, with the same aberration coefficients.

APPENDIX: PHASE SPACE AND WIGNER FUNCTION FOR FINITE SYSTEMS

The Wigner function of the signal does not contain more information than the complex signal itself, but reveals its structure better, as Figs. 4 and 7 suggest. The construction of the standard Wigner function [28,29] can be made through asking for the covariance under phase-space translations between the classical function $F=\exp(\xi x+\eta p)$ and the operator $\mathcal{F}=\exp i(\xi\mathcal{X}+\eta\mathcal{P})$. The corresponding Wigner operator is then obtained by integrating their product $F^*\mathcal{F}$ over the manifold $(\xi,\eta)\in\mathfrak{R}^2$. The expectation value of this operator in a state $\psi(x)$ is the Wigner function $W(\psi|x,p)$.

For the rotation group $\mathsf{SO}(3)$, we [11,13] ask for covariance between the classical function on this group, written in polar coordinates (ρ,θ,ϕ):

$$R(\rho,\theta,\phi;x,p,\kappa):=\exp[-i(ux+vp+w\kappa)],\qquad \times\begin{cases}u=\rho\sin\theta\sin\phi,\\ v=\rho\sin\theta\cos\phi,\\ w=\rho\cos\theta,\end{cases} \tag{A1}$$

and the $N\times N$ unitary matrix function on the same group,

$$\mathbf{R}(\rho,\theta,\phi):=\exp[-i(u\mathbf{X}+v\mathbf{P}+w\mathbf{K})], \tag{A2}$$

which produces a rotation through the angle ρ around the axis $\hat{n}(\theta,\phi)$. The matrices representing Eq. (A2) are given by Wigner Big-D matrices [17], which carry the linear action of $\mathsf{SO}(3)$ on the space of N-point signals [9,10,23].

To introduce covariance between Eqs. (A1) and (A2), we build their bilinear generating function, integrating $R^*\mathbf{R}$ over $\{\rho,\theta,\phi\}\in\mathsf{SO}(3)$ with the appropriate invariant measure. This yields the "Wigner matrix" function

$$\mathbf{W}(x,p,\kappa) := \int_{\mathsf{SO}(3)} \mathrm{d}(\rho,\theta,\phi) \times \exp i[u(x-\mathbf{X}) + v(p-\mathbf{P}) + w(\kappa-\mathbf{K})], \quad \text{(A3)}$$

which is unitary and self-adjoint. We called $(x,p,\kappa) \in \mathfrak{R}^3$ the metaphase space of $\mathsf{SO}(3)$. The result separates into a factor depending only on the square radius of the sphere $x^2+p^2+\kappa^2 = r^2$ and a factor depending only on the spherical coordinates (β,γ) of this space, given by

$$p = r\sin\beta\sin\gamma, \qquad \kappa = r\sin\beta\cos\gamma, \qquad x = r\cos\beta. \quad \text{(A4)}$$

Note that, since we decided to have position diagonal, the x axis took the role of the "north z pole" that is traditional for polar coordinates, as shown in Fig. 8.

The squared radius r^2 in Eq. (A4) corresponds to the Casimir operator [Eq. (15)] whose value is $j(j+1)$. This implies that the significant range is $j < r < j+1$, and that we can fix r to some value in that interval (we chose $j+\frac{1}{2}$) and remain with a Wigner matrix function of (β,γ) [11]. For a given signal N-vector $\mathbf{f} = \{f_m\}_{m=-j}^{j}$, the $\mathsf{SO}(3)$–Wigner function will be the expectation value of Eq. (A3) in that state:

$$W_{\mathsf{SO}(3)}(\mathbf{f}|\beta,\gamma) := \mathbf{f}^\dagger \mathbf{W}(\beta,\gamma)\mathbf{f} = \sum_{m,m'=-j}^{j} f_m^* W_{m,m'}(\beta,\gamma) f_{m'}. \quad \text{(A5)}$$

The integral that gives the matrix elements $W_{m,m'}(\beta,\gamma)$ in Eq. (A3) can be performed over the sphere (θ,ϕ) using known properties of the Big-D Wigner rotation matrices [11], and reduced to the form

$$W_{m,m'}(\beta,\gamma) = e^{-i(m-m')\gamma} \sum_{\bar{m}=-j}^{j} d^j_{m,\bar{m}}(\beta)\bar{W}^j_{\bar{m}} d^j_{\bar{m},m'}(-\beta), \quad \text{(A6)}$$

where $\bar{W}^j_{\bar{m}}$ is a diagonal matrix, whose elements are calculated through an integral [11] that can be solved algebraically or numerically. These N constants we have called the Wigner constants need to be found once and for all in each dimension $N = 2j+1$.

Drawing functions on spheres is inconvenient, especially since the interesting part occurs around the lowest energy region $\kappa \approx -r$, where the sphere is tangent to the classical phase space $(x,p) \in \mathfrak{R}^2$, i.e., at the bottom pole of Fig. 8. For this reason, we project the sphere onto a rectangle (β,γ), as shown in Figs. 4 and 7. We note that the integration over the γ coordinate of the rectangle will yield the marginal that reproduces the absolute squares of the signal points [11].

The standard Wigner function [29] has the property of being in general slightly negative in small regions of phase space, except for Gaussian coherent states, when it is strictly positive. This property does not hold for the $\mathsf{SO}(3)$–Wigner function; for the Kravchuk coherent states on the sphere, it has small negative values in a region around the antipode, which becomes smaller as j grows. For the concrete case of the signal $(0,0,\ldots,0,1)$, namely $\Upsilon^j_{\pi/2}(x_m)$, whose phase-space maximum is at the $\beta = 0$ x pole, only the matrix element $W_{jj}(\beta,\gamma)$ in Eq. (A5) needs calculation; in Eq. (A6), this is done in terms of the Wigner coefficients $\bar{W}^j_{\bar{m}}$. At the antipode $\beta = \pi$, the value of the Wigner function is simply given by $\bar{W}^j_{-j}$. Numerical computation for $j = 5, 10, 15$ yields values -7.8260×10^{-5}, -5.5235×10^{-6}, -1.1366×10^{-6} in a smoothly decreasing trend.

ACKNOWLEDGMENTS

We acknowledge the support of the Óptica Matemática projects DGAPA-UNAM IN-105008 and SEP-CONACYT 79899, and we thank G. Krötzsch (Instituto de Ciencias Físicas, Universidad Nacional Autónoma de México) for his careful help with the graphics.

REFERENCES

1. K. B. Wolf, "Refracting surfaces between fibers," J. Opt. Soc. Am. A **8**, 1389–1398 (1991).
2. K. B. Wolf, "Linear transformations and aberrations in continuous and in finite systems," J. Phys. A **41**, 304026 (2008).
3. H. M. Ozaktas, Z. Zalevsky, and M. A. Kutay, *The Fractional Fourier Transform with Applications in Optics and Signal Processing* (Wiley, 2001).
4. Ç. Candan, M. A. Kutay, and H. M. Ozaktas, "The discrete fractional Fourier transform," IEEE Trans. Signal Process. **48**, 1329–1337 (2000).
5. A. Koç, H. M. Ozaktas, C. Candan, and M. A. Kutay, "Digital computation of linear canonical transforms," IEEE Trans. Signal Process. **56**, 2383–2394 (2008).
6. S.-C. Pei and C.-C. Tseng, "Discrete fractional Fourier transform based on orthogonal projections," IEEE Trans. Signal Process. **47**, 1335–1348 (1999).
7. J. J. Healy and J. T. Sheridan, "Fast linear canonical transforms," J. Opt. Soc. Am. A **27**, 21–30 (2010).
8. K. B. Wolf, *Geometric Optics on Phase Space* (Springer, 2004).
9. N. M. Atakishiyev and K. B. Wolf, "Fractional Fourier-Kravchuk transform," J. Opt. Soc. Am. A **14**, 1467–1477 (1997).
10. N. M. Atakishiyev, G. S. Pogosyan, and K. B. Wolf, "Finite models of the oscillator," Phys. Part. Nucl. **36**, 521–555 (2005).
11. N. M. Atakishiyev, S. M. Chumakov, and K. B. Wolf, "Wigner distribution function for finite systems," J. Math. Phys. **39**, 6247–6261 (1998).
12. S. T. Ali, N. M. Atakishiyev, S. M. Chumakov, and K. B. Wolf, "The Wigner 23 function for general Lie groups and the wavelet transform," Ann. Henri Poincaré **1**, 685–714 (2000).
13. A. J. Dragt, "Lie algebraic theory of geometrical optics and optical aberrations," J. Opt. Soc. Am. **72**, 372–379 (1982).
14. A. J. Dragt, E. Forest, and K. B. Wolf, "Foundations of a Lie algebraic theory of geometrical optics.," in *Lie Methods in Optics*, Lecture Notes in Physics (Springer, 1986), Vol. 250, pp. 105–158.
15. K. B. Wolf, "Discrete systems and signals on phase space," Appl. Math. Inf. Sci. **4**, 141–181 (2010).
16. R. Gilmore, *Lie Groups, Lie Algebras, and Some of Their Applications* (Wiley-Interscience, 1978).
17. L. C. Biedenharn and J. D. Louck, *Angular Momentum in Quantum Physics*, *Encyclopedia of Mathematics and Its Applications* (Addison-Wesley, 1981), Vol. 8.
18. N. M. Atakishiyev, L. E. Vicent, and K. B. Wolf, "Continuous vs. discrete fractional Fourier transforms," J. Comput. Appl. Math. **107**, 73–95 (1999).
19. M. Krawtchouk, "Sur une généralization des polinômes d'Hermite," C. R. Acad. Sci. Paris Ser. IV **189**, 620–622 (1929).
20. A. F. Nikiforov, S. K. Suslov, and V. B. Uvarov, *Classical Orthogonal Polynomials of a Discrete Variable*, Springer Series in Computational Physics (Springer, 1991).
21. N. M. Atakishiyev and S. K. Suslov, "Difference analogs of the harmonic oscillator," Theor. Math. Phys. **85**, 1055–1062 (1990).
22. N. M. Atakishiyev, G. S. Pogosyan, and K. B. Wolf, "Contraction of the finite one-dimensional oscillator," Int. J. Mod. Phys. A **18**, 317–327 (2003).
23. K. B. Wolf and G. Krötzsch, "Geometry and dynamics in the fractional discrete Fourier transform," J. Opt. Soc. Am. A **24**, 651–658 (2007).
24. S. H. Cheng, N. J. Higham, C. S. Kenney, and A. J. Laub, "Approximating the logarithm of a matrix to a specified accuracy," SIAM J. Matrix Anal. Appl. **22**, 1112–1125 (2001).

25. L. M. Nieto, N. M. Atakishiyev, S. M. Chumakov, and K. B. Wolf, "Wigner distribution function for Euclidean systems," J. Phys. A **31**, 3875–3895 (1998).
26. C. A. Muñoz, J. Rueda-Paz, and K. B. Wolf, "Discrete repulsive oscillator wavefunctions," J. Phys. A **42**, 485210 (2009).
27. K. B. Wolf and G. Krötzsch, "Metaxial correction of fractional Fourier transformers," J. Opt. Soc. Am. A **16**, 821–830 (1999).
28. E. P. Wigner, "On the quantum correction for thermodynamic equilibrium," Phys. Rev. **40**, 749–759 (1932).
29. H.-W. Lee, "Theory and applications of the quantum phase-space distribution functions," Phys. Rep. **259**, 147–211 (1995).